Enhanced High-Temperature Thermoelectric Performance of Yb 4 Sb 3 via Ce/Bi Co-doping and Metallic Contact Deposition for Device Integration

Sylvain Le Tonquesse, Hugo Bouteiller, Yoshitaka Matsushita, Araseli Cortez, Sabah Bux, Kazuki Imasato, Michihiro Ohta, Jean-François Halet, Takao Mori, Franck Gascoin, et al.

Enhanced high-temperature thermoelectric performance of Yb_4Sb_3 via Ce/Bi co-doping and metallic contact deposition for device integration

Sylvain Le Tonquesse,[*,†,‡] Hugo Bouteiller,[†,‡] Yoshitaka Matsushita,[¶] Araseli Cortez,[§] Sabah K. Bux,[§] Kazuki Imasato,[‖,⊥] Michihiro Ohta,[‖] Jean-François Halet,[‡] Takao Mori,[#] Franck Gascoin,[†] and David Berthebaud[*,‡,@]

†*Normandie Université, ENSICAEN, UNICAEN, CNRS, CRISMAT, 14000, Caen, France*

‡*CNRS-Saint-Gobain-NIMS, IRL 3629, Laboratory for Innovative Key Materials and Structures (LINK), National Institute for Materials Science, Tsukuba 305-0044, Japan*

¶*National Institute for Materials Science, 1-2-1 Sengen, Tsukuba, Ibaraki, 305-0047, Japan*

§*Thermal Energy Conversion Research and Advancement Group, Jet Propulsion Laboratory, California Institute of Technology, 4800 Oak Grove Drive, Pasadena, CA 91109-8099, USA*

‖*Global Zero Emission Research Center, National Institute of Advanced Industrial Science and Technology (AIST), Umezono 1-1-1, Tsukuba, Ibaraki 305-8568, Japan*

⊥*Max Planck Institute for Chemical Physics of Solids, Nöthnitzer Str. 40, 01187 Dresden, Germany*

#*National Institute for Materials Science (NIMS), WPI-MANA, 1-1-1 Namiki, Tsukuba 305-0044, Japan*

@*Nantes Université, CNRS, Institut des Matériaux de Nantes Jean Rouxel, IMN, F-44000 Nantes, France*

E-mail: sylvain.le-tonquesse@ensicaen.fr; david.berthebaud@cnrs.fr

Abstract

Thermoelectrics (TE) for very high temperatures (> 800 K) have numerous potential applications in the heavy industry and the space exploration. This article focuses on the compound Yb_4Sb_3 which is a promising *p*-type counterpart to the structurally related and high-performance *n*-type RE_3Te_4 (RE = Nd, La, Pr) for the fabrication of high temperature TE modules. A quick and efficient method for synthesizing pure and fully-dense Yb_4Sb_3 samples was developed and optimized using high-energy ball milling followed by reactive spark plasma sintering. The technique was utilized to produce a series of doubly doped $Ce_xYb_{4-x}Bi_{0.2}Sb_{2.8}$ compounds. X-ray diffraction and scanning electron microscopy (SEM) were employed to establish the solubility limit of Ce, which was determined to be $x = 0.4$. TE properties of Yb_4Sb_3 and $Ce_{0.4}Yb_{3.6}Bi_{0.2}Sb_{2.8}$ were measured up to 1273 K, revealing that the doping strategy was effective in reducing the charge carrier concentration and thermal conductivity. This led to a significant increase in the TE figure of merit zT from 0.2 to 0.4 at 1273 K. In addition, screening of metallic contact was conducted for the development of thermoelectric module with Yb_4Sb_3. The results showed that two robust TE legs with Ni and Cu contacts were successfully produced through SPS sintering. The measured electric contact resistances were very promising, with average values of 2 and 1 $\mu\Omega$ cm^2 for Ni and Cu contacts, respectively.

Keywords

Thermoelectrics, Intermetallics, Electric contacts, Ball-milling, High temperature

1 Introduction

Thermoelectric (TE) generators are reliable solid-state devices that take advantage of the Seebeck effect to produce electrical energy from a temperature gradient. Typically, TE generators consist of two TE compounds with opposite *n*- and *p*-types electrical conduction,

which are connected electrically in series but thermally in parallel.[1] The conversion efficiency of the device is directly related to the figures of merit zT of the individual materials which is given by:

$$zT = \frac{\alpha^2 T}{\rho\kappa} \tag{1}$$

with α the Seebeck coefficient, ρ the electrical resistivity, κ the thermal conductivity and T the absolute temperature. These intrinsic properties of materials vary with temperature and are optimized differently for each material. Thus, the choice of TE materials to make a generator primarily depends on the operational temperature of the target application. Previous researches have primarily focused on materials suitable for near room-temperature applications (300 - 400 K), such as Bi_2Te_3[2] or Mg_3Bi_2,[3] or for mid-temperature applications (600 - 800 K), such as PbTe,[4,5] skutterudite $CoSb_3$,[6,7] transition metal silicides[8,9] or SnSe.[10,11] Nonetheless, fewer studies have been devoted to high-temperature applications (1000 - 1200 K) despite their significant potential in heavy industry and space exploration. Si-Ge alloys have historically been the most investigated materials for high-temperature applications,[12] but new materials exhibiting promising properties have emerged, such as the Zintl phase $Yb_{14}MSb_{11}$ (M = Mg, Mn),[13,14] Heusler alloys[15] or borides.[16,17] However, to improve the industrial potential of TE generators in this temperature range, new materials demonstrating superior performance and stability need to be discovered.

Refractory rare earth tellurides crystallizing in the cubic Th_3P_4 structure-type are another class of promising high temperature TE materials. $La_{3-x}Te_4$, a compound that can accommodate large vacancies concentration on the La site, has long been known to show $zT \approx 1.1$ at 1273 K for an optimized vacancy concentration of $x = 0.23$.[18] Recently, the isostructural compounds $Nd_{2.78}Te_4$[19] and $Pr_{2.74}Te_4$[20] were reported to have even higher zT values of 1.2 and 1.7 at 1273 K, respectively. These materials exhibit good TE properties due to (i) the relatively low κ caused by the presence of vacancies, (ii) the rare earth $4f$ orbitals

forming a heavy band near the Fermi level in the electronic density of states (DOS) and resulting in relatively high α and (iii) the strong correlation between the vacancy concentration x and the charge carrier concentration n, allowing for easy optimization of the power factor $PF = \alpha^2/\rho$. The relationship between vacancy concentration and electronic properties of these materials can be intuitively understood by considering the charge balanced formulation $(RE^{3+})_{3-x}(Te^{2-})_4(e^-)_{1-3x}$ where an excess of electrons (e^-) is necessary to compensate vacancies formation on the rare earth (RE) sub-lattice, which results in n-type electronic conduction. Interestingly, no p-type counterpart with similar properties has been discovered yet, which limits their integration in thermoelectric generators.

Yb_4Sb_3 which crystallizes in the anti-Th_3P_4 structure type, in which the anionic and cationic sub-lattices are reversed compared to the Th_3P_4 structure type, is a good candidate showing p-type electrical conduction. Unlike rare earth tellurides just mentioned above, Yb_4Sb_3 is stoichiometric and cannot accommodate large vacancy concentration on any of its cationic and anionic sub-lattices. Yb valence fluctuation is known to occur in this compound, with most studies indicating that the great majority of the Yb atoms are in a valence state of 2+ as determined by magnetic and X-ray absorption spectroscopy measurements.[21,22] The charge balanced formula can therefore be written as $(Yb^{2+})_4(Sb^{3-})_3(h^+)$ which correctly predicts an excess of positive charge carriers (h^+) and therefore the p-type conduction of this compound. Yb_4Sb_3 was reported to exhibit low resistivity in the order of 10 $\mu\Omega\ m$ at 1273 K due to its elevated hole concentration in the order of 10^{21} cm^{-3} and a positive Seebeck coefficient beyond 500 K that reaches about 80 $\mu V\ K^{-1}$.[23] However, despite its potential, the thermal conductivity and zT of pristine Yb_4Sb_3 has not been reported in the literature to date. Nevertheless, studies have investigated the effect of doping of Yb_4Sb_3, where Yb was substituted with La,[24] Sm,[25] Ce or Eu,[26] and Sb with Bi[23] or I.[26] However, it should be noted that the thermoelectric properties of most of these doped compounds were only partially reported, and Hall measurements were rarely performed. Based

on these partial results, doping with these elements seems to decrease the charge carrier concentration, but simultaneously increase α and ρ, resulting in an enhanced PF.[23,25] The substitution also significantly reduces the thermal conductivity due to the induced atomic disorder on the crystallographic sites.[24] As a direct consequence, a figure of merit zT as high as 0.75 at 1273 K was reported, for example, for the composition $La_{0.5}Yb_{3.5}Sb_3$.[24] Indeed, the promising thermoelectric performance of singly doped Yb_4Sb_3 compounds could potentially be improved further by co-doping, which involves simultaneous substitutions on both Yb and Sb sub-lattices. This approach aims to increase the concentration of electron donor elements while simultaneously increasing the atomic disorder to reduce the thermal conductivity. However, the synthesis of Yb_4Sb_3 reported in literature was conducted using a conventional high-temperature process in expensive Nb sealed tubes, which required several annealing steps at temperatures as high as 1323 K over a total of two weeks. To enable industrial applications for this compound, more cost-efficient and scalable synthesis processes need to be developed.

This article reports the synthesis of undoped Yb_4Sb_3 and doubly doped $Ce_xYb_{4-x}Bi_{0.2}Sb_{2.8}$ (x = 0.4, 0.5) compounds through a ball-milling step followed by a reactive spark plasma sintering (SPS) step. The solubility limit of Ce in the series $Ce_xYb_{4-x}Sb_3$ was previously reported as $x = 0.4$, with the Ce oxidation state of +3 on the basis of magnetic measurements.[26] Therefore, Ce shows promises as a dopant for decreasing the charge carrier concentration according to the $(Ce^{+3})_x(Yb^{2+})_{4-x}(Sb^{3-})_3(h^+)_{1-x}$ formalism. The Bi concentration of $y = 0.2$ was selected because it yields the highest properties in the $Yb_4Bi_ySb_{3-y}$ series.[25] Thermoelectric properties of the synthesized single-phased and fully-densified materials were measured up to 1273 K and are presented and discussed. Additionally, the high-temperature thermal expansion and oxidation behavior of pristine Yb_4Sb_3 are discussed, as these properties are crucial for industrial applications. Additionally, preliminary results for the fabrication of a TE leg are presented, involving the deposition of Ni and Cu metallic contacts on Yb_4Sb_3

using a direct SPS process.

2 Experimental part

2.1 Synthesis

Pristine Yb_4Sb_3 and substituted $Ce_xYb_{4-x}Bi_{0.2}Sb_{2.8}$ ($x = 0.4$, 0.5) samples were synthesized from pure elements, Yb (ingot, 99.9 %, Alfa Aesar), Ce (ribbon, 99.9 %, Alfa Aesar), Sb (shot, 99.999 %, Sigma-Aldrich) and Bi (shot, 99.999 %, Sigma-Aldrich), using a two-step process combining high-energy ball-milling and reactive SPS. The rare earth metal ingots were first cleaned with a file inside a glove box ($O_2 < 1$ ppm, $H_2O < 1$ ppm) to removed the oxide layer at the surface. Stoichiometric amounts of metal precursors were weighed, except for Yb which was added with a 2 % excess due to its tendency to adhere to the milling jar's walls. About 3.5 g of metal precursor mixtures were loaded inside a 65 mL hardened steel grinding jar with two Ø = 12.6 mm hardened steel grinding balls (weighing 7 g in total) under Ar atmosphere. The mixtures were ball-milled for 8 h using a SPEX 8000M Mixer apparatus. The resulting powders, black in color and highly sensitive to air, were recovered within the glove box. The powders underwent reactive sintering using a Dr. Sinter Lab. SPS-322Lx apparatus in a Ø = 10 mm graphite die. The sintering process was carried out at 1573 K for 10 min with a uniaxial pressure of 50 MPa under dynamic vacuum. The heating and cooling ramps were set to 40 K min^{-1}. The uniaxial pressure was set before the heating ramp and released slowly during the cooling ramp. Finally, the densified pellets were wrapped in a 0.05 mm thick Ta foil and annealed in evacuated silica tubes (10^{-3} mbar) for 24 h at 1273 K.

Ni and Cu powders were utilized for the electrical contact fabrication on pristine Yb_4Sb_3. The Ni powder (particle size below 45 μm, 99.5 %, Sigma-Aldrich) and Cu powder (particle size of 150 μm, 99.9 %, Sigma-Aldrich) were arranged in a layered succession with the ball-milled Yb-Sb powder mixture inside a Ø = 10 mm graphite die. Firstly, metal powder (250

mg for Ni, 200 mg for Cu) was placed evenly at the bottom of the graphite die, followed by the Yb-Sb ball-milled mixture (1.5 g), and finally another identical layer of metal powder. The whole set-up was cold pressed at 50 MPa inside a glove-box to ensure good contact between the different layers during the sintering. The sintering steps were performed under an uniaxial pressure of 50 MPa and under dynamic vacuum at 1373 K for 20 min for Ni and 1173 K for 20 min for Cu. The sintering temperature was lowered in the case of Cu to avoid melting the metal contact. The heating and cooling ramps were set to 40 K min^{-1}. The uniaxial pressure was set before the heating ramp and released slowly during the cooling ramp. Finally, the obtained Ni/Yb_4Sb_3/Ni and Cu/Yb_4Sb_3/Cu pellets with thickness of about 2 mm were polished to remove the covering graphite foil and cut into 5×5 mm^2 square-shaped pellets using a diamond wire saw.

2.2 Material characterizations

X-ray diffraction (XRD) analyses were conducted on powders obtained by grinding parts of the annealed SPS-sintered pellets using a mortar and pestle inside the glove-box. Room-temperature XRD patterns were carried out using a Rigaku SmartLab diffractometer (Cu radiation, $\lambda_{K\alpha1}$ = 1.54056 Å and $\lambda_{K\alpha2}$ = 1.5444 Å with an intensity ratio $\lambda_{K\alpha2}/\lambda_{K\alpha1}$ of 0.5) with scanning step size of 0.02°. The high-temperature XRD measurements were performed with a Rigaku SmartLab diffractometer (Cu rotating target, monochromatized incident beam $\lambda_{K\alpha1}$ = 1.54056 Å) equipped with a D/teX Ultra 250 detector. The patterns were measured from 300 to 900 K every 50 K under Ar flow (1 L min^{-1}, 5N purity) with a scanning step size of 0.02° and using variable slits. The powder was only exposed a brief time to air (< 1 min) during the positioning of the Al_2O_3 sample holder inside the diffractometer furnace chamber, which was then purged three times with Ar before the measurement. The X-ray powder patterns were fitted using the FullProf software.[27] The peak shapes were modeled using Thompson-Cox-Hastings pseudo-Voigt functions.[28] Berar's factors were applied to the estimated standard deviations to obtain more realistic values.[29] Scanning electron microscope

(SEM) back-scattered electron images of the polished pellet surfaces were taken using a Hitachi Tabletop Microscope TM3000. The EDS chemical compositions were estimated by averaging between 4 and 8 point analyses per samples. In the case of $Ce_{0.5}Yb_{3.5}Bi_{0.2}Sb_{2.8}$, the analyses were performed exclusively on the main phase, excluding the secondary CeSb phase. The SEM analyses of the TE leg cross-sections were performed using a Jeol 7200LV apparatus equipped with a Bruker X-Flash60 EDS detector.

2.3 Thermoelectric properties measurements

Thermal diffusivity (D) measurements were performed under N_2 atmosphere (99.999 %) on $\varnothing = 10$ mm and 2 mm thick pellets coated with graphite using the laser flash analysis (LFA) apparatus Netzsch 467 HyperFlash. The thermal conductivity (κ_{tot}) was calculated using the expression $\kappa_{tot} = D\ C_p\ d$ with d the density and C_p the specific heat. The thermal dependence of C_p was estimated using a Netzsch *Pyroceram* reference during the thermal diffusivity measurements. It was found to increase approximately linearly from 0.17 to 0.20 J g^{-1} K^{-1} from 298 to 1270 K, respectively. d was determined by the Archimede method in absolute ethanol. The lattice thermal conductivity κ_L was estimated by subtracting the electronic contribution κ_E, calculated using the Wiedemann-Franz relationship $\kappa_E = L\ T/\rho$ with $L = 2.44\ 10^{-8}$ W Ω K^{-2}, to κ_{tot}. The electrical resistivity (ρ) and the Hall coefficient (R_H) were measured using the van der Pauw method on a custom-built system under dynamic vacuum (10^{-5} mbar).[30] The measurements were carried out on a $\varnothing = 10$ mm pellet shaped sample with a thickness of about 1 mm. The charge carrier concentration (n) and mobility (μ) were calculated from the R_H measurements realized under a magnetic field of 0.75 T using the relations (2) and (3), respectively.

$$n = \frac{1}{R_H e} \quad (2) \qquad \mu = \frac{R_H}{\rho} \quad (3)$$

with e the elemental charge of the electron. The Seebeck coefficient (α) was measured with a custom-built instrument using the light pulse method under dynamic vacuum (10^{-5} mbar).[31] Scanning resistance measurements across the Yb_4Sb_3 leg with Cu and Ni metal contacts were performed at room temperature in air using a home-made apparatus described elsewhere.[32]

3 Results and discussion

The finely divided powder mixture obtained after ball milling exhibited high reactivity, allowing for simultaneous reaction and sintering at a relative density exceeding 99 % in only 10 min at 1573 K. This alternative approach using high-energy ball milling offers the advantages of significantly reducing the thermal treatment duration and being more scalable than conventional fusion-solidification processes. It should be noted that after sintering, the pellets displayed weak mechanical stability and are prone to breakage during cutting or high-temperature measurements. To enhance their mechanical integrity, an additional annealing step at 1273 K for 24 h was implemented. The precise effect of this annealing step is not yet fully understood, as the density, grain size, and chemical composition of the samples were found to be similar before and after annealing. Another observation is the slow oxidation of the sintered samples when stored in air, indicated by the progressive darkening of their initially shiny metallic surface within a few hours. To minimize oxidation, the samples discussed in this study were stored in a glove box, with exposure to air minimized as much as possible.

Table 1: Nominal compositions, experimental compositions determined by SEM-EDS, absolute and relative densities of the sintered samples Yb_4Sb_3, $Ce_{0.4}Yb_{3.6}Bi_{0.2}Sb_{2.8}$ and $Ce_{0.5}Yb_{3.5}Bi_{0.2}Sb_{2.8}$

Nominal composition	SEM-EDS analyses	Density (g cm^{-3})	Relative density (%)
Yb_4Sb_3	$Yb_{4.10(5)}Sb_{2.90(4)}$	8.64	99.6
$Ce_{0.4}Yb_{3.6}Bi_{0.2}Sb_{2.8}$	$Ce_{0.41(3)}Yb_{3.68(5)}Bi_{0.20(2)}Sb_{2.71(4)}$	8.43	99.0
$Ce_{0.5}Yb_{3.5}Bi_{0.2}Sb_{2.8}$	$Ce_{0.46(3)}Yb_{3.64(5)}Bi_{0.18(2)}Sb_{2.72(4)}$	8.28	98.2

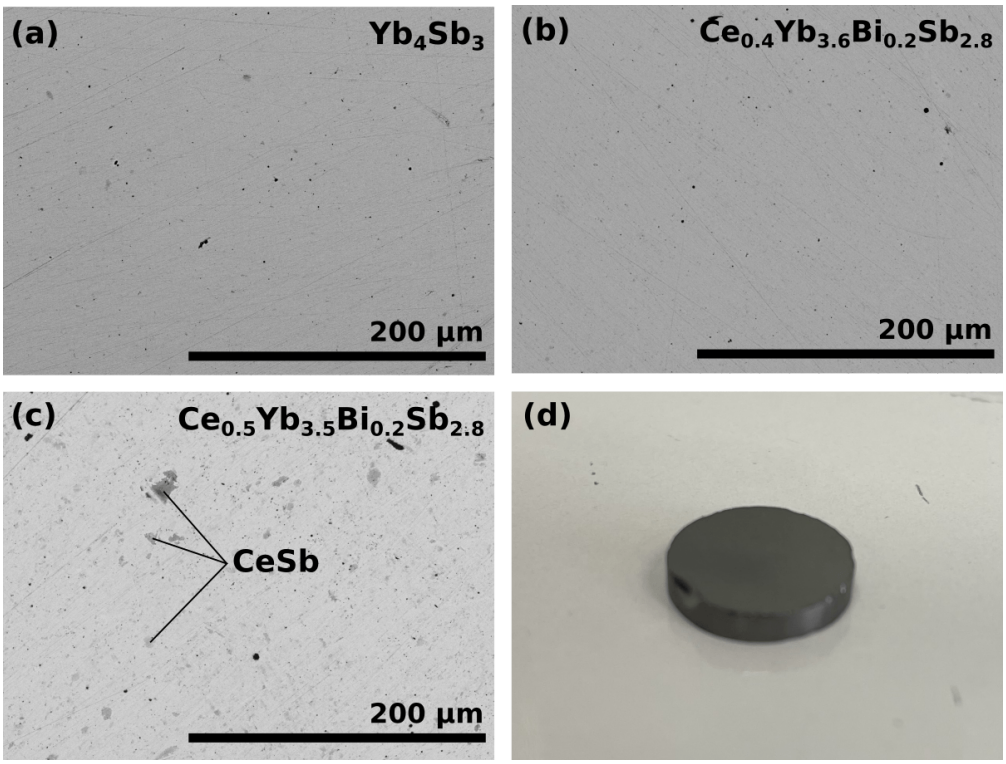

Figure 1: SEM back-scattered electrons images of the polished surface of (a) Yb_4Sb_3, (b) $Ce_{0.4}Yb_{3.6}Bi_{0.2}Sb_{2.8}$ and (c) $Ce_{0.5}Yb_{3.5}Bi_{0.2}Sb_{2.8}$, (d) picture of a sintered pellet of Yb_4Sb_3 after the annealing step showing a shiny metallic aspect

Figures 1 and Table 1 show SEM back-scattered electron images and SEM-EDS analyses conducted on the polished surface of the annealed sintered pellets, respectively. The absence of chemical contrast on the surface of Yb_4Sb_3 and $Ce_{0.4}Yb_{3.6}Bi_{0.2}Sb_{2.8}$ indicates a good chemical homogeneity. Only a low amount of porosity is visible on the surface which aligns with the high relative densities of the samples reported in Table 1. Most importantly, the chemical compositions determined by EDS analyses are in good agreement with the targeted nominal compositions. However, the back-scattered electron image of $Ce_{0.5}Yb_{3.5}Bi_{0.2}Sb_{2.8}$ reveals the presence of an impurity (dark gray area) that was identified as CeSb by EDS analysis. The formation of less dense CeSb (6.37 g cm^{-3}) compared to Yb_4Sb_3 (8.67 g cm^{-3}) can explain the lower relative density of this sample.

Yb_4Sb_3 adopts the anti-Th_3P_4 structure type ($I\bar{4}3d$, no. 220) as illustrated in Figure

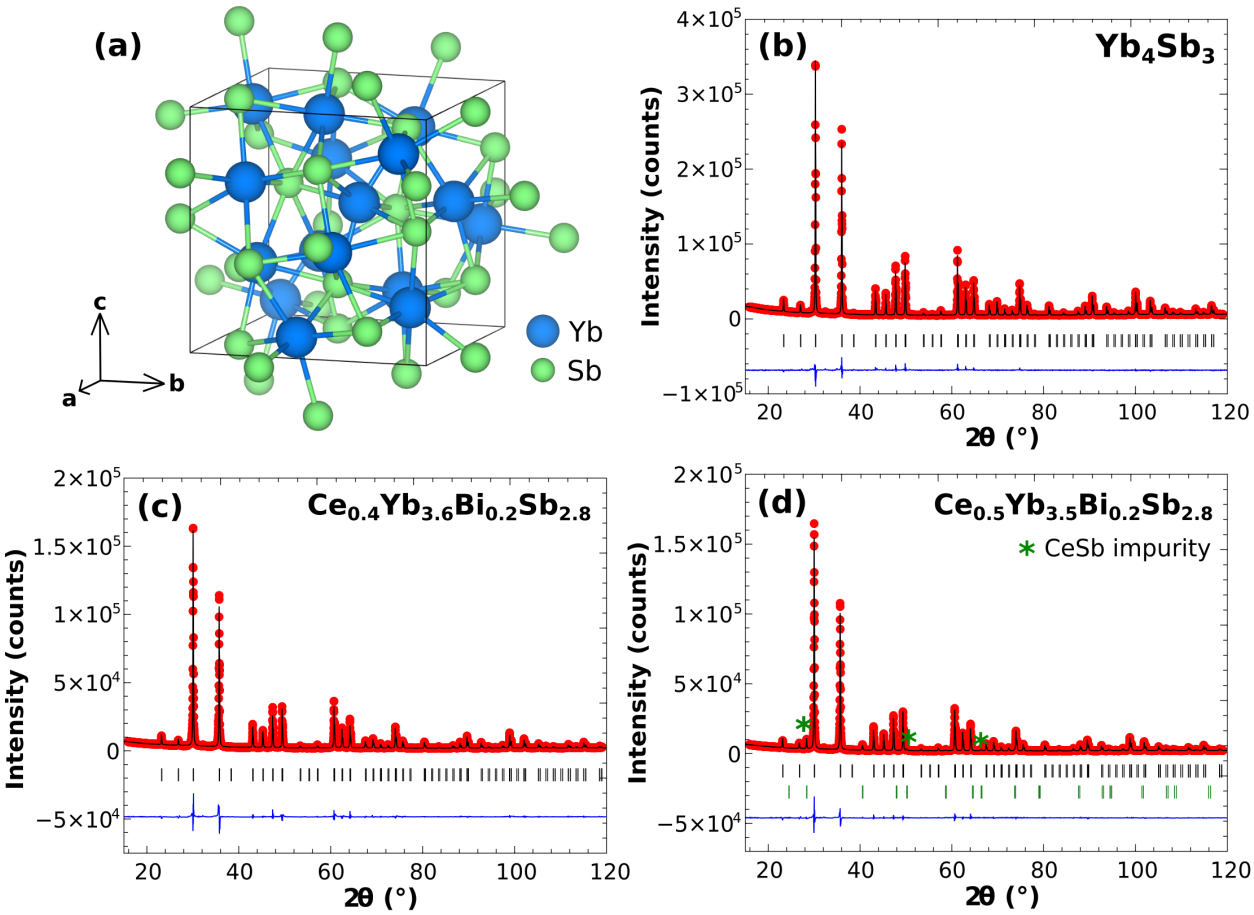

Figure 2: (a) crystal structure of Yb_4Sb_3 and Rietveld refined XRD patterns of (b) Yb_4Sb_3, (c) $Ce_{0.4}Yb_{3.6}Bi_{0.2}Sb_{2.8}$ and (d) $Ce_{0.5}Yb_{3.5}Bi_{0.2}Sb_{2.8}$. The experimental data are plotted in red symbols, the calculated pattern with a black line and the difference with a blue line. The vertical ticks indicate the theoretical Bragg positions of Yb_4Sb_3 (black) and CeSb impurity (green).

2(a). The unit cell is composed of 28 atoms (Z = 4), with Yb occupying the 16*c* Wyckoff site and Sb occupying the 12*a* Wyckoff site. Figures 2(b,c,d) shows the Rietveld refined XRD powder patterns measured on crushed sintered pellets after annealing. Table 2 lists the obtained refined structural parameters. Consistent with the SEM analyses, the diffraction patterns of Yb_4Sb_3 and $Ce_{0.4}Yb_{3.6}Bi_{0.2}Sb_{2.8}$ are single-phased with all diffraction peaks successfully indexed with the Th_3P_4 structure type. However, the diffraction pattern of $Ce_{0.5}Yb_{3.5}Bi_{0.2}Sb_{2.8}$ shows additional small peaks corresponding to some CeSb impurity ($Fm\bar{3}m$, no. 225), corroborating the findings from the SEM analyses. The refined

Table 2: Structural parameters and R factors obtained by Rietveld refinement of Yb_4Sb_3, $Ce_{0.4}Yb_{3.6}Bi_{0.2}Sb_{2.8}$ and $Ce_{0.5}Yb_{3.5}Bi_{0.2}Sb_{2.8}$ XRD patterns. Single (*) and double stars (**) indicate fixed (non-refined) and constrained occupancy parameters (*Occ. Yb* = 1 - *Occ. Ce* on the 16*c* site and *Occ. Sb* = 1 - *Occ. Bi* on the 12*a* site)

	Yb_4Sb_3	$Ce_{0.4}Yb_{3.6}Bi_{0.2}Sb_{2.8}$	$Ce_{0.5}Yb_{3.5}Bi_{0.2}Sb_{2.8}$
a (Å)	9.3228(2)	9.3997(2)	9.4106(1)
		Wyckoff site 16*c* (*x*,*x*,*x*)	
x	0.0732(3)	0.0728(5)	0.0728(3)
Occ. Ce	-	0.1(1)	0.12(9)
Occ. Yb	1*	0.9**	0.88**
B_{iso} (Å^2)	0.5(1)	1.0(1)	0.6(1)
		Wyckoff site 12*a* (3/8, 0, 1/4)	
Occ. Bi	-	0.10(5)	0.11(3)
Occ. Sb	1*	0.90**	0.89**
B_{iso} (Å^2)	0.5(1)	0.9(1)	0.6(1)
		R factors	
χ^2	4.45	5.67	4.62
R_{Bragg}	2.02	2.85	2.15

lattice parameter$a$ = 9.3228(2) Å for Yb_4Sb_3 agrees relatively well with a previous study reporting a = 9.321(5) Å.[23] Upon doping, the refined lattice parameter increased to a = 9.3997(2) Å and 9.4106(1) Å for $Ce_{0.4}Yb_{3.6}Bi_{0.2}Sb_{2.8}$ and $Ce_{0.5}Yb_{3.5}Bi_{0.2}Sb_{2.8}$, respectively. This increase is consistent with the larger atomic radii of the substituting elements, Ce (185 pm) and Bi (160 pm), compared to Yb (175 pm) and Sb (145 pm), respectively.[33]

The presence of CeSb impurity in $Ce_{0.5}Yb_{3.5}Bi_{0.2}Sb_{2.8}$, as confirmed by both XRD and SEM, and the limited increase in lattice parameter upon further Ce addition in $Ce_{0.4}Yb_{3.6}Bi_{0.2}Sb_{2.8}$ suggest that the solubility limit of Ce in this system is slightly above x = 0.4. This finding is consistent with previously reported values for the $Ce_xYb_{4-x}Sb_3$ series synthesized through conventional high-temperature synthesis methods. It suggests that the substitution with Bi on the Sb site has a minimal effect on the solubility limit of Ce.[26] It is important to note

that the anti-Th_3P_4 crystal structure features large cavities located at the 12*b* Wyckoff site (7/8, 0, 1/4), which can accommodate interstitial atoms like Au in $Au_3Y_3Sb_4$.[34] However, in this study, the structural model used, where all Ce and Bi atoms substitute Yb and Sb on their respective sites, shows a good agreement with experimental data. The main source of discrepancy between the measured and calculated data (blue line in Figure 2(b,c,d)) is primarily attributed to the asymmetric shape of the more intense peaks, which could not be fully captured in the refinements. The free atomic parameters of the Yb atoms on the 16*c* site, regardless of the chemical composition, were found to be similar and consistent with a previously reported value of $x = 0.074(1)$.[35] The refined chemical compositions for the doped compounds, $Ce_{0.40(4)}Yb_{3.60}Bi_{0.3(1)}Sb_{2.7}$ and $Ce_{0.5(3)}Yb_{3.50}Bi_{0.3(1)}Sb_{2.7}$, which were obtained by constraining the 16*c* and 12*a* sites to full occupancy, are in good agreement with both the nominal compositions and the compositions determined by SEM-EDS analyses.

Yb_3Sb_4 is aimed to be used for ultra high-temperature TE applications, making the characterization of its structure and stability under operating condition of great interest. Figure 3(a) shows the high temperature XRD patterns of powdered Yb_3Sb_4 sintered pellet collected at intervals of 50 K from 300 to 900 K. The initial pattern at 300 K mostly shows the Yb_3Sb_4 phase with contribution of the Al_2O_3 sample support. Additional peaks in the 31-33° 2θ region appeared at 550 K, which are attributed to the low temperature phase of Yb_5Sb_3 ($P6_3/mcm$, no. 193). From 650 K onwards, the decomposition of Yb_4Sb_3 accelerates with a significant decrease in peak intensities and the appearance of broad peaks associated with elemental Sb ($R\bar{3}m$, no. 166) and Yb_2O_3 ($Ia\bar{3}$, no. 206). At 800 K, the Yb_4Sb_3 and Yb_5Sb_3 intermetallic phases completely disappear and only Sb and Yb_2O_3 remained. The progressive decomposition of the Yb_4Sb_3 phase is attributed to its oxidation caused by residual oxygen absorbed at the surface of the sample particles or in the experimental set-up. It demonstrates that this phase is extremely sensible to oxidation above 500 K even in an environment where air was thoroughly purged. While this extreme oxidation behavior poses

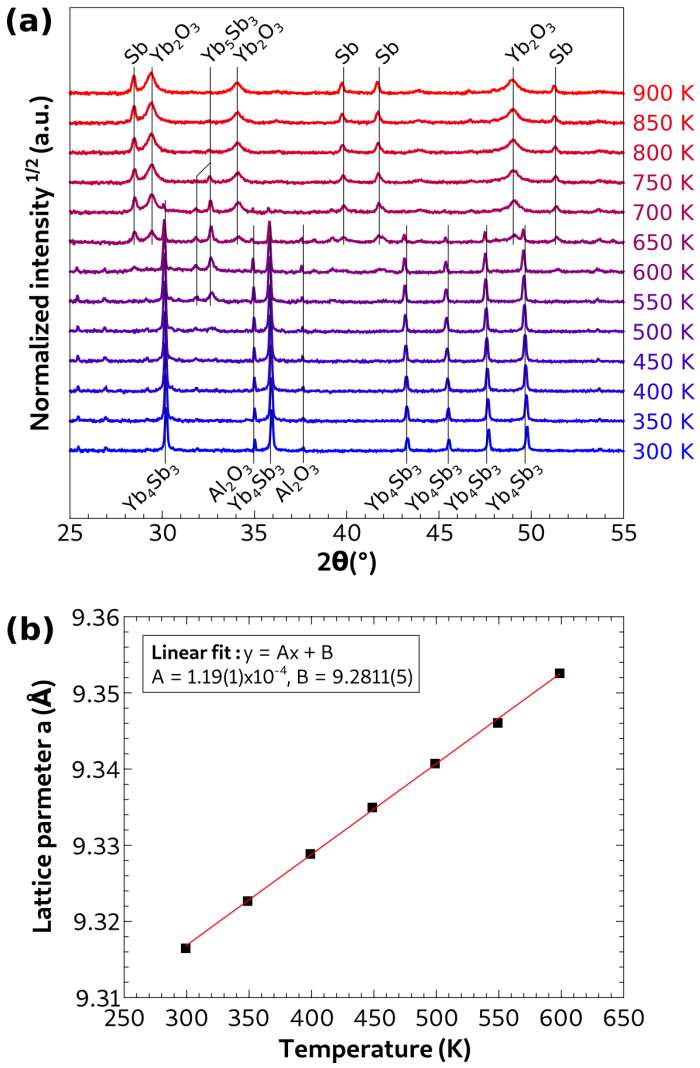

Figure 3: (a) High temperature XRD patterns of Yb_3Sb_4 measured up to 900 K, and (b) the thermal evolution of the refined lattice parameter up to 600 K. The error bars on the lattice parameter values are smaller than the symbols.

challenges for many terrestrial applications, it is not a primary concern for space applications where oxygen is absent and high operating temperatures are required. Le Bail refinements were performed on the XRD patterns from 300 to 600 K, and the refined lattice parameters are presented in Figure 3(b). The thermal evolution follows a linear trend allowing the calculation of the linear thermal expansion parameter of $12.7(6)\times10^{-6}$ K^{-1} at 300 K. The determination of this parameter holds great significance for the realization of metallic contacts, which will be discussed further below.

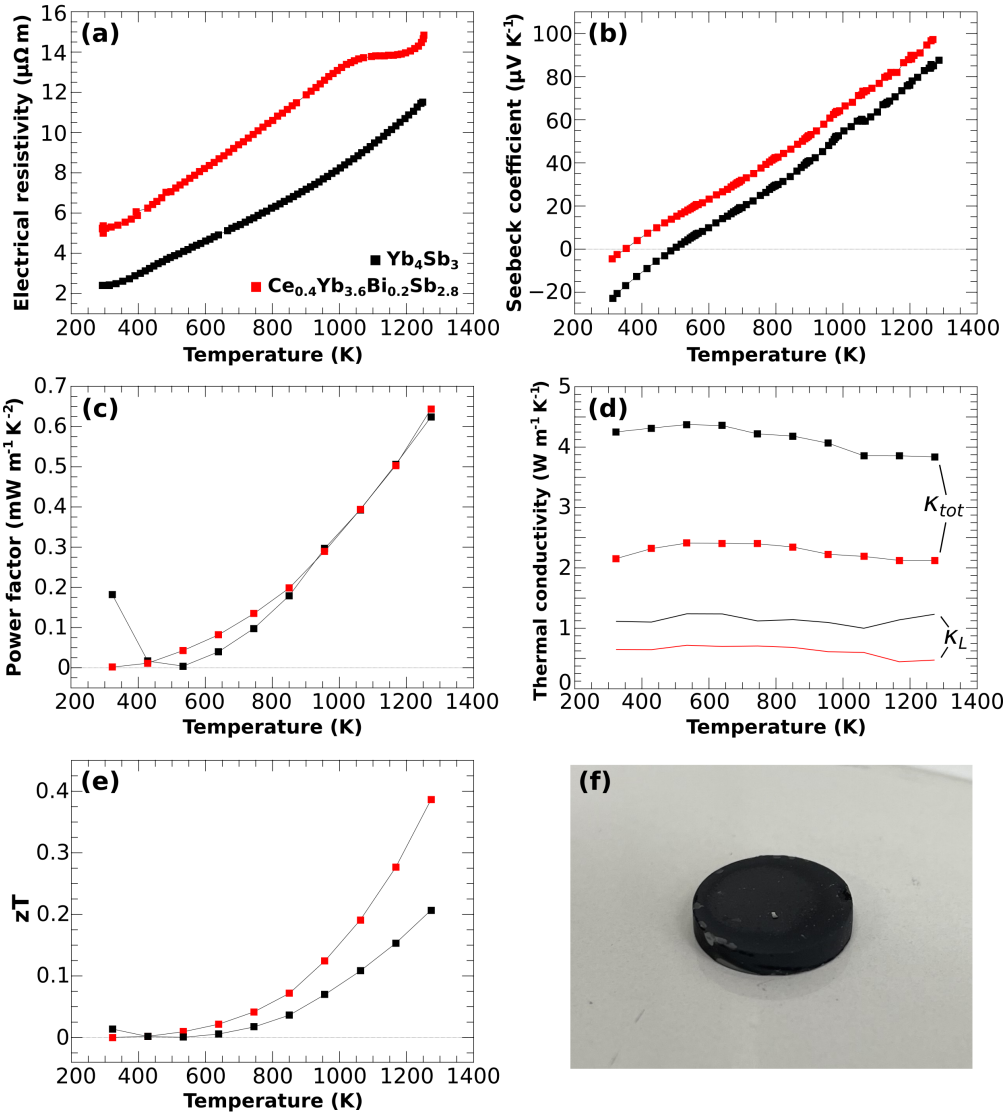

Figure 4: High-temperature thermoelectric properties of Yb_4Sb_3 (black) and $Ce_{0.4}Yb_{3.6}Bi_{0.2}Sb_{2.8}$ (red): (a) electrical resistivity, (b) Seebeck coefficient, (c) power factor, (d) total (symbols) and lattice (solid lines) thermal conductivities, and (e) figure-of-merit zT. (f) Picture of a sintered pellet of Yb_4Sb_3 after the thermal conductivity measurement showing an oxidized surface

The TE properties of the single-phased samples with nominal compositions Yb_4Sb_3 and $Ce_{0.4}Yb_{3.6}Bi_{0.2}Sb_{2.8}$ were investigated from 298 to 1273 K. Figures 4(a) and 4(b) shows the electrical resistivity and Seebeck coefficient measurements, respectively. The pristine sample exhibits a metallic behavior, with the electrical resistivity increasing from 2 to 12 $\mu\Omega$ m

as the temperature rises from 298 to 1273 K. The Seebeck coefficient displays a consistent upward trend, starting from a negative value of -20 μV K^{-1} at 298 K, indicating an n-type electrical behavior. It changes to p-type behavior at around 500 K, eventually reaching a maximum of 85 μV K^{-1} at 1273 K. Such a change of the electrical behavior from n to p-type was already reported multiple times in the literature at similar temperatures.[24,36] From Hall measurements conducted at 298 K, a charge carrier concentration of 3.0×10^{21} cm^{-3} and a mobility of 9.5 cm^2 V^{-1} s^{-1} were determined. These values are in good agreement with a previous study and are consistent with the observed metallic behavior of this compound.[21] The Seebeck coefficient of the present sample is significantly higher at high temperatures than the previously reported value of 65 μV K^{-1} at 1273 K for pristine Yb_4Sb_3 synthesized through conventional high-temperature synthesis.[25] However, the electrical resistivity remains in excellent agreement across the entire temperature range. The exact reason for this discrepancy is not yet fully understood, but it could potentially be attributed to differences in microstructure or undetectable contamination resulting from the utilization of different synthesis methods. Doping with Ce and Bi leads to an increase in both the electrical resistivity and the Seebeck coefficient, resulting in maximum values of 15 $\mu\Omega$ m (+ 30 %) and 100 μV K^{-1} (+ 18 %) at 1273 K, respectively. This increase can be directly attributed to the decrease in charge carrier concentration to 1.8×10^{21} cm^{-3} as a result of Yb^{2+} substitution with Ce^{3+}. The doping also has a slight effect on the charge carrier mobility, which decreases to 6.4 cm^2 V^{-1} s^{-1}. Despite the successful doping, the resulting power factors (PF) shown in Figure 4(c) remain comparable for the two samples with a maximum value of 0.65 mW m^{-1} K^{-2} at 1273 K. In comparison, the stoichiometric n-type counterparts materials La_3Te_4, Pr_3Te_4 and Nd_3Te_4 only show slightly superior PF in the range 0.7 to 1.0 mW m^{-1} K^{-2} at the same temperature.[18–20] However, in these cases, the decrease in charge carrier concentration can be successfully achieved by creating vacancies on the rare earth site, resulting in strongly enhanced PF values greater than 1.5 mW m^{-1} K^{-2}.[20] For instance, a comparable reduction in charge carrier concentration from 4.0 to 2.0×10^{21} cm^{-3}

by going from the compositions $Nd_{2.9}Te_4$ to $Nd_{2.86}Te_4$ leads to a significant 40 % increase of the PF.[19] The optimization of the charge carrier concentration is essential to achieve a substantial boost of the TE properties of the n-type rare earth tellurides but it does not appear to hold for the present p-type Yb_4Sb_3 system.

Figure 4(b) presents the total (κ_{tot}) and the estimated lattice (κ_L) thermal conductivities measure for the two compositions. The undoped sample Yb_4Sb_3, which was measured for the first time to the best of our knowledge, exhibits κ_{tot} values going from 4.2 W m^{-1} K^{-1} at 298 K to 3.8 W m^{-1} K^{-1} and 1273 K. Similar weak temperature dependence is observed for the stoichiometric n-type compounds Pr_3Te_4 and Nd_3Te_4, with slightly lower κ_{tot} values around 3.5 W m^{-1} K^{-1}.[19,20] The estimated electronic thermal conductivity (κ_E) was found to represent about 70 % of κ_{tot}, which is consistent with the high charge carrier concentration of this compound. The estimated κ_L remains constant at approximately 1.2 W m^{-1} K^{-1} throughout the temperature range. This relatively low κ_L value can be attributed to the complex crystal structure and the presence of heavy constituting elements in Yb_4Sb_3. Upon doping, κ_{tot} is significantly reduced by more than 40 %, reaching a value of about 2.2 W m^{-1} K^{-1} across the entire temperature range. The decrease in κ_{tot} is partially attributed to the reduction of κ_E consecutive to the reduced charge carrier concentration in the doped compound. Furthermore, κ_L is significantly reduced by about 50 % to reach approximately 0.6 W m^{-1} K^{-1} over the entire temperature range. This reduction of κ_L is directly related to the introduction of atomic disorder in the structure due to partial substitution on both crystallographic sites. Such a significant reduction in κ_L is generally advantageous for improving the thermoelectric performance of materials since it is the only parameter in the figure of merit zT that is not correlated with the charge carrier concentration.

Finally, Figure 4(e) displays the figure of merit zT values for both the pristine and doped samples. At temperatures below 800 K, zT is small for both samples due to the low absolute

Seebeck coefficients. However, zT increases rapidly at higher temperatures. For the first time to our knowledge, a maximum zT of 0.21 is achieved for the pristine sample at 1273 K. As a direct consequence of the induced structural disorder, $Ce_{0.4}Yb_{3.6}Bi_{0.2}Sb_{2.8}$ exhibits a significantly improved zT of 0.39 (+85 %), primarily due to the substantial reduction in the thermal conductivity. The measured zT values obtained for the investigated compositions, although significant, remained lower than the reported values of approximately 0.75 for $La_{0.5}Yb_{3.5}Sb_3$ and 0.65 for $Sm_{0.4}Yb_{3.6}Sb_3$.[24] This difference in properties is attributed to the higher Seebeck coefficient observed in these compositions, which reached 120 μV K^{-1} at 1273 K. Further investigations are required to gain a better understanding of the influence of the various doping elements and synthesis processes on the Seebeck coefficient of these materials. It is worth noting that during the TE property measurements at the highest temperatures, the surface of the samples undergoes significant oxidation. This oxidation is evident in Figure 4(f), which shows the initially shiny metallic surface turning black after the measurement. The oxidation process poses challenges in accurately measuring the transport properties due to the deterioration of electrical contact quality. This is believed to be the cause of the slight deviations observed in the electrical resistivity data of the doped sample above 1100 K in Figure 4(a). However, the measurement of the transport properties for both samples showed reversibility upon heating/cooling cycle as shown in Figure S1. Moreover, it should be emphasized that the oxidized layer is confined to the surface of the pellet and can be effectively removed by polishing after the measurements, restoring the sample to its original condition.

The deposition of metallic contacts on TE materials is crucial for their successful integration into functional devices. This task presents several challenges as the contacts need to possess strong adhesion, low electrical and thermal interface resistances, and compatible thermal expansion properties with the TE material to prevent crack formation during synthesis and operation at high temperatures. To address these requirements, Ni (α =

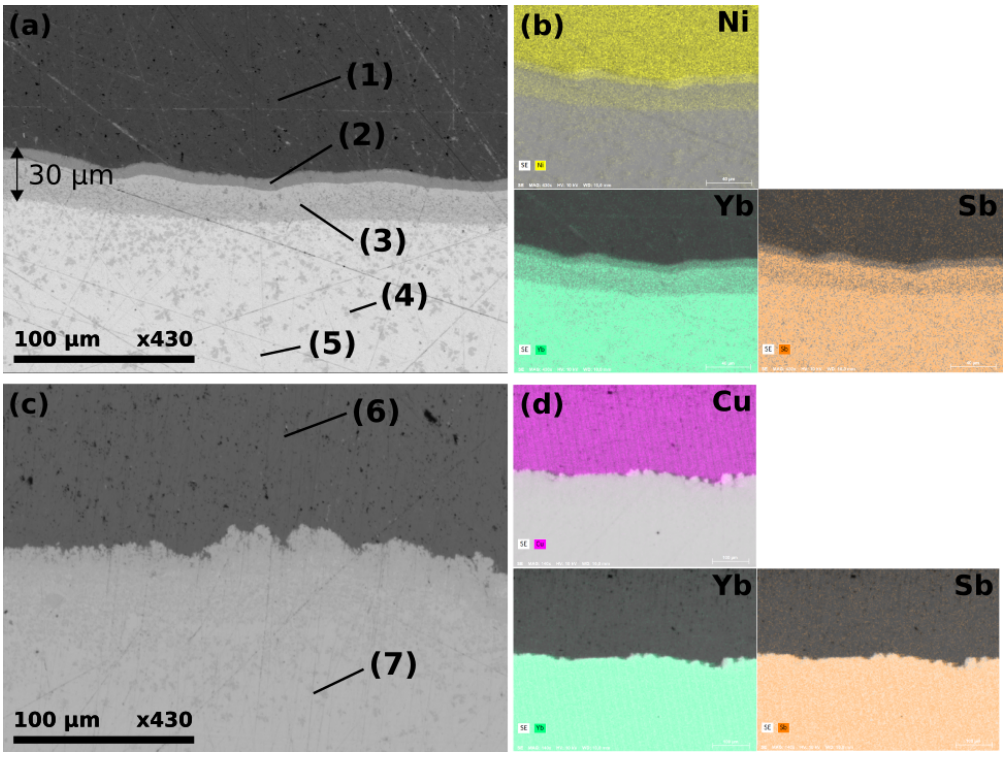

Figure 5: SEM back-scattered electron images of the contact interface and corresponding EDS mappings. The images (a,b) and (c,d) correspond to the legs with Ni and Cu contacts, respectively. EDS compositions of the phases indicated with numbers in (a) and (c) are given in Table 3

Table 3: SEM-EDS analyses of the different phases found at the contact interface of the Ni and Cu legs. The analysis numbers correspond to the areas indicated in Figure 5(a,c)

Analysis number	Ni (at.%)	Cu (at.%)	Yb (at.%)	Sb (at.%)	Attributed phase
(1)	98	-	1	1	Ni
(2)	69	-	21	10	$Ni_2Yb_{1-x}Sb_x$
(3)	39	-	33	28	YbNiSb
(4)	22	-	45	33	$Ni_{1-x}YbSb$
(5)	< 1	-	60	40	Yb_4Sb_3
(6)	-	94	3	3	Cu
(7)	-	< 1	60	40	Yb_4Sb_3

13.4×10^{-6} K^{-1}) and Cu ($\alpha = 16.5\times10^{-6}$ K^{-1}) were chosen due to their relatively close match with the thermal expansion parameter of Yb_4Sb_3 ($\alpha = 12.7\times10^{-6}$ K^{-1}) determined earlier by XRD. Figures 5(a,b) and 5(c,d) display representative SEM back-scattered electron images and corresponding EDS mappings of the contact interfaces for Ni and Cu, respectively.

The elemental composition of the interface phases were determined by EDS analyses, and the results are presented in Table 3. In both cases, the contact interfaces exhibited no cracks or excessive porosity which is consistent with the good mechanical properties of the legs. For the Ni contacts shown in Figure 5(a), two distinct phases (2) and (3) were observed at the interface between Ni and Yb_4Sb_3, which correspond to the phase (1) and (5), respectively. The EDS mapping revealed that both phases are composed of the three elements, with a decrease in Ni concentration from the metal contact to the TE phase. Composition of the phase (2) suggests that it may be the Laves phase Ni_2Yb ($MgCu_2$ structure-type, $Fd\bar{3}m$, no. 227), potentially with some Sb substitution on the Yb site. However, to the best of our knowledge, such a substitution has not been reported in the literature, and no Ni_2Sb phase is reported in the Ni-Sb phase diagram. Phase (3) is identified as the half-Heusler YbNiSb ($F\bar{4}3m$, no. 216), which is the only known ternary compound in this system. Additionally, the presence of darker spots with sizes below approximately 5 μm, visible within the Yb_4Sb_3 matrix, corresponds to phase (5). This phase, composed of the three elements, exhibits a relatively lower Ni content compared to phase (4). It may be attributed to Ni-deficient $Ni_{1-x}YbSb$ as already reported by R. Mishra *et al.*[37] However, it should be noted that the EDS measurement accuracy for this phase may be compromised due to the relatively small size of the analyzed area, which can include some part of the Yb_4Sb_3 matrix owing to the interaction volume of the electron beam (a few μm). In the case of Cu contacts shown in Figure 5(c,d), no formation of new phases was observed at the interface between Cu and Yb_4Sb_3, which corresponds to phases (6) and (7), respectively. The EDS mapping clearly indicates a sharp separation of the elements at the interphase, indicating the absence of significant interdiffusion. The formation of several new phases at the interface with Ni, which are absent for Cu, are expected to contribute to increase the electrical and thermal contact resistances of the TE legs.

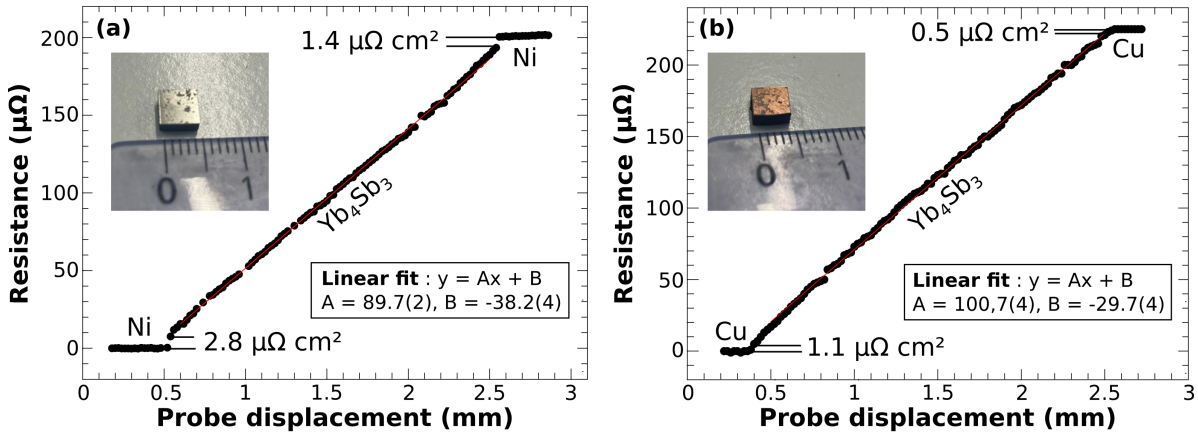

Figure 6: Room temperature scanning electrical resistance measurements of the (a) Ni and (b) Cu legs. The pictures in inset show the samples used for the measurements.

The electrical contact resistivities measured at room temperature for the Ni and Cu legs are shown in Figures 6(a) and 6(b), respectively. The contact resistivity was estimated from the jump of the electrical resistance occurring between the metal contact and TE materials. For the Ni leg, contact resistivities of 2.8 and 1.4 $\mu\Omega$ cm^2 were measured, while for the Cu leg, contact resistivities of 1.1 and 0.5 $\mu\Omega$ cm^2 were obtained. These values, ranging in the order of a few $\mu\Omega$ cm^2, indicate good electrical contact quality.[38] The higher contact resistivities observed for the Ni leg compared to the Cu leg are consistent with the formation of secondary phases observed in the SEM analyses. The electrical resistivity of Yb_4Sb_3 in the legs was estimated to be 2.2 and 2.5 $\mu\Omega$ m based on the slope of the linear section. These values are of the same order of magnitude as the room temperature value of 2.4 $\mu\Omega$ shown in Figure 4(a). The slight deviation is attributed to the density change resulting from different sintering temperatures used for the leg synthesis. This confirms that there is no significant diffusion of the metal contact into the TE material, which would otherwise affect its electronic properties.[39]

4 Conclusion

Single phased and fully densified Yb_4Sb_3 materials were successfully synthesized via ball milling followed by reactive SPS. However, two challenges were encountered for the samples obtained. Firstly, they exhibited mechanical fragility, necessitating annealing at 1273 K for 24 hours. Secondly, they demonstrated high sensitivity to oxidation above 550 K, even in a purged protective atmosphere, which posed difficulties in measuring the high-temperature TE properties. A new series of doubly substituted $Ce_xYb_{4-x}Bi_{0.2}Sb_{2.8}$ samples were synthesized. Despite the substitution with Bi on the Sb site, XRD and SEM analyses revealed an unchanged Ce solubility limit of $x = 0.4$, consistent with the previously reported singly doped $Ce_xYb_{4-x}Sb_3$ series. The substitution of Yb^{2+} with Ce^{3+} effectively reduced the charge carrier concentration of $Ce_{0.4}Yb_{3.6}Bi_{0.2}Sb_{2.8}$ resulting in an slightly increased Seebeck coefficient compared to pristine Yb_4Sb_3. However, this improvement was accompanied by an increase in electrical resistivity, leading to a comparable maximum PF of approximately 0.4 mW m^{-1} K^{-2} at 1273 K for both samples. Nonetheless, the introduction of atomic disorder through the double substitution significantly decreased the lattice thermal conductivity, resulting in an improved zT of 0.4 (+ 50 %) at 1273 K. Based on the determined linear thermal expansion coefficient of 12.7×10^{-6} K^{-1} from high-temperature XRD measurements, Cu and Ni were selected as metal contacts to fabricate TE legs using SPS. Low averaged electric contact resistances of 2 and 1 $\mu\Omega$ cm^2 were measured for Ni and Cu, respectively. These promising results highlight the potential of these materials for fabricating TE devices intended for high-temperature applications.

Supporting Information Available

- TE-reversible.png: Heating-cooling cycle measurements of the electrical resistivity and Seebeck coefficient of undoped Yb_4Sb_3 and $Ce_{0.4}Yb_{3.6}Bi_{0.2}Sb_{2.8}$

Acknowledgement

The authors thank the *Agence Nationale de la Recherche* (ANR) for the funding ANR-18-CE05-0037. Hugo Bouteiller thanks Japan Society for the Promotion of Science (JSPS) (Grant number PE21708). Part of the research was carried out at the Jet Propulsion Laboratory, California Institute of Technology, under a contract with the National Aeronautics and Space Administration (80NM0018D0004). Xavier Larose (CRISMAT laboratory) is acknowledged for SEM images and EDS analyses performed on the thermoelectric legs. Part of the researchwas carriedoutat the Jet PropulsionLaboratory,CaliforniaInstituteofTechnology,undera contractwiththe NationalAeronauticsand SpaceAdministration(80NM0018D0004).

References

(1) Hendricks, T.; Caillat, T.; Mori, T. Keynote Review of Latest Advances in Thermoelectric Generation Materials, Devices, and Technologies 2022. *Energies* **2022**, *15*, 7307.

(2) El Oualid, S.; Kosior, F.; Dauscher, A.; Candolfi, C.; Span, G.; Mehmedovic, E.; Paris, J.; Lenoir, B. Innovative Design of Bismuth-telluride-based Thermoelectric Micro-generators with High Output Power. *Energy Environ. Sci.* **2020**, *13*, 3579–3591.

(3) Liu, Z.; Gao, W.; Oshima, H.; Nagase, K.; Lee, C.-H.; Mori, T. Maximizing the Performance of n-type Mg_3Bi_2 based Materials for Room-temperature Power Generation and Thermoelectric Cooling. *Nat. Commun.* **2022**, *13*, 1120.

(4) Jood, P.; Male, J. P.; Anand, S.; Matsushita, Y.; Takagiwa, Y.; Kanatzidis, M. G.; Snyder, G. J.; Ohta, M. Na Doping in PbTe: Solubility, Band Convergence, Phase Boundary Mapping, and Thermoelectric Properties. *J. Am. Chem. Soc.* **2020**, *142*, 15464–15475.

(5) Wang, X.; Veremchuk, I.; Burkhardt, U.; Bobnar, M.; Böttner, H.; Kuo, C.-Y.;

Chen, C.-T.; Chang, C.-F.; Zhao, J.-T.; Grin, Y. Thermoelectric Stability of Eu- and Na-substituted PbTe. *J. Mater. Chem. C* **2018**, *6*, 9482–9493.

(6) El Oualid, S.; Kogut, I.; Benyahia, M.; Geczi, E.; Kruck, U.; Kosior, F.; Masschelein, P.; Candolfi, C.; Dauscher, A.; Koenig, J. D.; Jacquot, A.; Caillat, T.; Alleno, E.; Lenoir, B. High Power Density Thermoelectric Generators with Skutterudites. *Adv. Energ. Mater.* **2021**, *11*, 2100580.

(7) Le Tonquesse, S.; Alleno, E.; Demange, V.; Prestipino, C.; Rouleau, O.; Pasturel, M. Reaction Mechanism and Thermoelectric Properties of $In_{022}Co_4Sb_{12}$ Prepared by Magnesiothermy. *Mater. Today Chem.* **2020**, *16*, 100223.

(8) Le Tonquesse, S.; Joanny, L.; Guo, Q.; Elkaim, E.; Demange, V.; Berthebaud, D.; Mori, T.; Pasturel, M.; Prestipino, C. Influence of Stoichiometry and Aging at Operating Temperature on Thermoelectric Higher Manganese Silicides. *Chem. Mater.* **2020**, *32*, 10601–10609.

(9) Le Tonquesse, S.; Zhang, W.; Srinivasan, B.; Fontaine, B.; Hiroto, T.; Mori, T.; Halet, J.-F.; Berthebaud, D.; Suzuki, T. S. Improvement of Thermoelectric Properties via Texturation Using a Magnetic Slip Casting Process-The Illustrative Case of $CrSi_2$. *Chem. Mater.* **2022**, *34*, 1143–1156.

(10) Chandra, S.; Dutta, P.; Biswas, K. High-Performance Thermoelectrics Based on Solution-Grown SnSe Nanostructures. *ACS Nano* **2022**, *16*, 7–14.

(11) Chandra, S.; Bhat, U.; Dutta, P.; Bhardwaj, A.; Datta, R.; Biswas, K. Modular Nanostructures Facilitate Low Thermal Conductivity and Ultra-High Thermoelectric Performance in n-Type SnSe. *Adv. Mater.* **2022**, *34*, 2203725.

(12) Scoville, N.; Bajgar, C.; Rolfe, J.; Fleurial, J.-P.; Vandersande, J. Thermal Conductivity Reduction in SiGe Alloys by the Addition of Nanophase Particles. *Nanostruc. Mater.* **1995**, *5*, 207–223.

(13) Brown, S. R.; Kauzlarich, S. M.; Gascoin, F.; Snyder, G. J. $Yb_{14}MnSb_{11}$: New High Efficiency Thermoelectric Material for Power Generation. *Chem. Mater.* **2006**, *18*, 1873–1877.

(14) Perez, C. J.; Cerretti, G.; Wille, E. L. K.; Devlin, K. P.; Grewal, N. S.; Justl, A. P.; Wood, M.; Bux, S. K.; Kauzlarich, S. M. Evolution of Thermoelectric Properties in the Triple Cation Zintl Phase: $Yb_{13-x}Ca_xBaMgSb_{11}$ (x = 1-6). *Chem. Mater.* **2021**, *33*, 8059–8069.

(15) Quinn, R. J.; Bos, J.-W. G. Advances in Half-Heusler Alloys for Thermoelectric Power Generation. *Mater. Adv.* **2021**, *2*, 6246–6266.

(16) Sauerschnig, P.; Tsuchiya, K.; Tanaka, T.; Michiue, Y.; Sologub, O.; Yin, S.; Yoshikawa, A.; Shishido, T.; Mori, T. On the Thermoelectric and Magnetic Properties, Hardness, and Crystal Structure of the Higher Boride YbB_{66}. *J. Alloys Compd.* **2020**, *813*, 152182.

(17) Mori, T. Perspectives of High-Temperature Thermoelectric Applications and p-type and n-type Aluminoborides. *JOM* **2016**, *68*, 2673–2679.

(18) May, A. F.; Fleurial, J.-P.; Snyder, G. J. Thermoelectric Performance of Lanthanum Telluride Produced via Mechanical Alloying. *Phys. Rev. B* **2008**, *78*, 125205.

(19) Gomez, J., Steven; Cheikh, D.; Vo, T.; Von Allmen, P.; Lee, K.; Wood, M.; Snyder, G. J.; Dunn, B. S.; Fleurial, J.-P.; Bux, S. K. Synthesis and Characterization of Vacancy-Doped Neodymium Telluride for Thermoelectric Applications. *Chem. Mater.* **2019**, *31*, 4460–4468.

(20) Cheikh, D.; Hogan, B. E.; Vo, T.; Von Allmen, P.; Lee, K.; Smiadak, D. M.; Zevalkink, A.; Dunn, B. S.; Fleurial, J.-P.; Bux, S. K. Praseodymium Telluride: A High-Temperature, High-ZT Thermoelectric Material. *Joule* **2018**, *2*, 698–709.

(21) Ochiai, A.; Nakai, S.; Oyamada, A.; Suzuki, T.; Kasuya, T. Valence Fluctuation in anti-Th_3P_4 Structure Yb_4Sb_3 and Yb_4Bi_3. *J. Magn. Magn. Mater.* **1985**, *47-48*, 570–572.

(22) Aoki, H.; Ochiai, A.; Suzuki, T.; Helfrich, R.; Steglich, F. Systematic Study in Mixed Valence System $Yb_4(As_{1-x}Sb_x)_3$. *Physica B* **1997**, *230-232*, 698–701.

(23) Chamoire, A.; Viennois, R.; Tedenac, J.-C.; Koza, M. M.; Gascoin, F. Antimony-Based Compounds with the Anti-Th_3P_4 Structure as Potential High-Temperature Thermoelectric Materials. *J. Electron. Mater.* **2011**, *40*, 1171–1175.

(24) Chamoire, A.; Gascoin, F.; Estournès, C.; Caillat, T.; Tédenac, J.-C. High-temperature Transport Properties of Complex Antimonides with Anti-Th_3P_4 Structure. *Dalton Trans.* **2010**, *39*, 1118–1123.

(25) Chamoire, A.; Gascoin, F.; Estournès, C.; Caillat, T.; Tédenac, J.-C. High-Temperature Transport Properties of $Yb_{4-x}Sm_xSb_3$. *J. Electron. Mater.* **2010**, *39*, 1579–1582.

(26) Chamoire, A. Antimoniures Complexes de Type Th_3P_4 et Propriétés Thermoélectriques. *Université Montpellier II - Sciences et Techniques du Languedoc* **2009**, (PhD thesis written in french).

(27) Rodriguez-Carvajal, J. Recent Advances in Magnetic-structure Determination by Neutron Powder Diffraction. *Physica B* **1993**, *192*, 55–69.

(28) Thompson, P.; Cox, D. E.; Hastings, J. B. Rietveld Refinement of Debye-Scherrer Synchrotron X-ray data from Al_2O_3. *J. Appl. Cryst.* **1987**, *20*, 79–83.

(29) Bérar, J.-F.; Lelann, P. E.s.d.'s and Estimated Probable Error Obtained in Rietveld Refinements with Local Correlations. *J. Appl. Cryst.* **1991**, *24*, 1–5.

(30) Borup, K. A.; Toberer, E. S.; Zoltan, L. D.; Nakatsukasa, G.; Errico, M.; Fleurial, J.-P.; Iversen, B. B.; Snyder, G. J. Measurement of the Electrical Resistivity and Hall Coefficient at High Temperatures. *Rev. Sci. Instrum.* **2012**, *83*, 123902.

(31) Wood, C.; Zoltan, D.; Stapfer, G. Measurement of Seebeck Coefficient using a Light Pulse. *Rev. Sci. Instrum.* **1985**, *56*, 719–722.

(32) Mengali, O.; Seiler, M. Contact Resistance Studies on Thermoelectric Materials. *Adv. Energy Convers.* **1962**, *2*, 59–68.

(33) Slater, J. C. Atomic Radii in Crystals. *J. Chem. Phys.* **1964**, *41*, 3199–3205.

(34) Dwight, A. E. Yttrium-gold-antimony $Y_3Au_3Sb_4$. *Acta Cryst.* **1977**, *B33*, 1579–1581.

(35) Bodnar, R. E.; Steinfink, H. The Phase Equilibria and Crystal Chemistry of the Intermediate Phases in the Ytterbium-Antimony System. *Inorg. Chem.* **1967**, *6*, 327–330.

(36) Bucher, E.; Cooper, A.; Jaccard, D.; Sierro, J. Valence Instabilities and Related Narrow Band Gap Phenomena. *P.D. Park (Plenum Press, New York)* **1977**, 529.

(37) Mishraa, R.; Pöttgen, R.; Hoffmann, R.-D.; Fickenscher, T.; Eschen, M.; Trill, H.; Mosel, B. D. Ternary Antimonides YbTSb (T = Ni, Pd, Pt, Cu, Ag, Au) – Synthesis, Structure, Homogeneity Ranges, and ^{121}Sb Mössbauer Spectroscopy. *Z. Naturforsch. B* **2002**, *57*, 1215–1223.

(38) He, R.; Schierning, G.; Nielsch, K. Thermoelectric Devices: A Review of Devices, Architectures, and Contact Optimization. *Adv. Mater. Technol.* **2018**, *3*, 1700256.

(39) Le Tonquesse, S.; Matsushita, Y.; Jood, P.; Ohta, M.; Mori, T.; Berthebaud, D. Fabrication and Evaluation of Low-Cost $CrSi_2$ Thermoelectric Legs. *Crystals* **2021**, *11*, 1140.

TOC Graphic

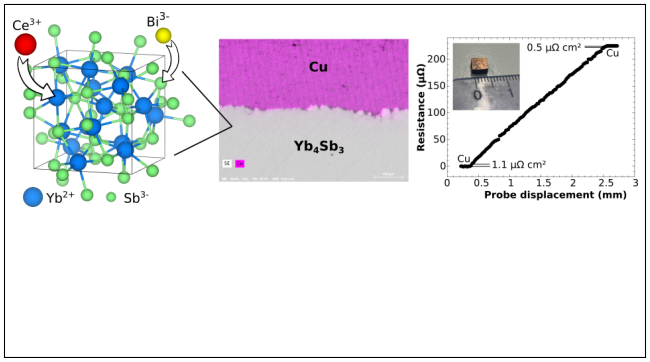
Ce3+
Bi3-
Yb2+
Sb3-
Cu
Yb4Sb3
0.5 μΩ cm²
Cu
1.1 μΩ cm²
Cu
Resistance (μΩ)
Probe displacement (mm)